

Optimization of momentum imaging systems using electric and magnetic fields

M. Gisselbrecht and A. Huetz

LIXAM, UMR 8624, Université Paris Sud, Bâtiment 350, Orsay Cedex, France

M. Lavollée

LURE, UMR 130, Université Paris Sud, Bâtiment 209D, Orsay Cedex, France

T. J. Reddish and D. P. Seccombe

Department of Physics, University of Windsor, Ontario, Canada N9B 3P4

(Received 4 August 2004; accepted 20 October 2004; published online 20 December 2004)

Time-of-flight (TOF) momentum imaging systems utilize the x , y , t information from charged particles striking a position-sensitive detector to infer the x , y , and z components of the particles' initial momenta. This measurement capability can lead to the complete experimental determination of multi-ionization/fragmentation dynamics. In the case of electron detection, the addition of a magnetic field leads to a significantly increased operational energy range. This study shows that the TOF system has to be carefully designed in order to optimize the magnetic confinement effect. Expressions for the optimal dimensions of a single electric field TOF system are derived and factors contributing to the resolution are discussed, along with their application to an existing imaging system. © 2005 American Institute of Physics. [DOI: 10.1063/1.1832411]

I. INTRODUCTION

The last two decades have seen the development of a variety of instruments that simultaneously utilize both position and time detection to probe gas-phase atomic and molecular dynamics.^{1–31} Usually these instruments consist of a conventional, linear time-of-flight (TOF) mass spectrometer fitted with a two-dimensional position-sensitive detector (PSD). Charged particles are extracted from the interaction region by an electric field, which is high enough to collect all possible trajectories (i.e., over 4π sr), and detected by the PSD. The measurement of their flight times (t) and impact positions (x, y) upon the detector yields all three components of their initial momenta (p_x , p_y , and p_z), and thereby provides kinematically complete information. In addition, the “multi-hit” capacity of certain detectors provides the opportunity to perform extremely powerful coincidence experiments. Lavollée¹⁵ has recently described the principles of operation for the types of detectors that are in current use with special emphasis on their multi-hit capability. In addition, Cold-Target Recoil Ion Mass Spectrometry (COLTRIMS), which represents a large subset of all the experiments performed, has been extensively reviewed.^{32,33}

All detection systems have a fundamental limit in the timing resolution (Δt_{\min}). This may be due to the pulse duration of the ionizing source, the capacitive effects of the physical detector, or the detector's associated electronics. In the case of synchrotron based experiments, it is often the latter issue that limits the timing resolution of the system, typically ~ 1 ns. Consequently, as ions have longer flight times than electrons and can therefore be analyzed with a much higher precision, it is more straightforward to investigate ion fragmentation dynamics (via measurement of ion-ion coincidences) than electron–electron correlation/

dynamics. Nevertheless, the *direct* measurement of the two electrons in photodouble ionization of helium [$h\nu + \text{He} \rightarrow \text{He}^{2+} + 2e^-$] has been successfully performed by Huetz and Mazeau³⁴ in the near threshold (< 200 meV) energy region. The same process has also been investigated using COLTRIMS, where one only detects one electron in coincidence with the recoil ion. The momentum of the other electron can be deduced from that of the detected electron and recoil ion using momentum conservation. However, the precision in the determination of the undetected electron's momentum is ultimately limited by the inherent initial energy spread of the cold target. Although this limits the lowest energy that one can study by this technique, COLTRIMS has provided a large amount of data on electron-electron dynamics at higher energies. More recently, detector improvements have enabled the direct detection of both electrons.

In general, the detection of high-energy electrons with 4π collection efficiency requires even higher “extraction” fields. These high fields reduce the flight time of the electrons, with the consequence that they cannot be detected with sufficient precision (as Δt_{\min} is fixed). In an effort to overcome this problem, some groups (e.g., Refs. 9, 13, and 31–33) have incorporated a uniform magnetic field parallel to the time-of-flight axis. Such a field provides a force, which essentially opposes the inherent radial expansion (due to the initial transverse momenta) of the electrons' trajectories as they traverse the time-of-flight spectrometer. This confinement of the electrons' radial extent is extremely valuable since it *reduces* the electric field strength required to detect electrons of a given energy with 4π collection efficiency. The overall effect, therefore, is an increased flight time, allowing analysis of higher energy electrons (in our case up to ~ 20 eV with a ~ 20 Gauss field, see Sec. III). Furthermore,

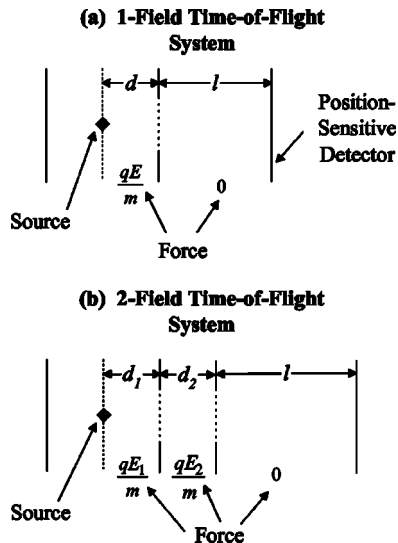


FIG. 1. Schematic diagrams of the 1 and 2 electric field TOF configurations along with the basic definitions of the lengths and forces used in the mathematical derivations.

this magnetic field (depending on its strength and the TOF size and electric field strengths) will not affect the ion trajectories significantly in a COLTRIMS or ion-electron coincidence experiments—and even this perturbation can be incorporated into the ion analysis.

There is the temptation to think that a magnetic field can simply be added to an existing electron TOF to attain the benefit of a higher energy range. However, the electron TOF spectrometer has to be carefully designed in order to gain the maximum benefit from the magnetic field. The purpose of this study is to provide the analytical details of incorporating a B field into a TOF geometry, as such information is not elaborated in the published literature. These principles will be highly valuable for designing an apparatus. First, the conditions required for optimal resolution will be derived (Sec. II), for the simplest case of a one-field TOF, i.e., a single electric “extraction” field, followed by an (electric) field-free region or “drift tube.” Second, the application of these principles to the pre-existing “CIEL” (*Coincidences entre Ions et Electrons Localisés*) apparatus¹⁵ will be described (Sec. III).

II. THEORY

A. 3D imaging spectrometer: 4π detection

In the first instance the interaction region is considered to be a point source located at the origin of a Cartesian coordinate system $(x, y, z=0, 0, 0)$. The electrons, once formed, are accelerated over a distance, d , by an electric field, $E(z)$, and subsequently move through a field-free region of length, l , before striking the position-sensitive detector of radius, R [see Fig. 1(a)]. In the rest of the article it will be assumed that the radius of the TOF system equals the radius of the detector, as is usually the case in such instruments. The electrons’ flight times (t), as well as their positions of impact on the detector [coordinates (x, y) , the center of the detector is located at $(0,0)$], are measured. These experimentally determined quantities and the known values of E , d , and l are

used to extract the three components of the electrons’ initial momenta (p_x , p_y , and p_z). In the absence of a magnetic field the (p_x, p_y) components are simply given by

$$p_x = \frac{mx}{t}, \quad (1)$$

$$p_y = \frac{my}{t}, \quad (2)$$

as there is no force component orthogonal to the z axis. The p_z component is contained within the following expression for t ,

$$t = \frac{\sqrt{p_z^2 + 2mqEd} - p_z}{qE} + \frac{lm}{\sqrt{p_z^2 + 2mqEd}}, \quad (3)$$

where m and q are the electron’s mass and charge, respectively. Equation (3) does not readily simplify to give a trivial solution for p_z , however, in the limit that $p_z \ll \sqrt{2mqEd}$ one can show that

$$p_z = qE(t - t_o), \quad (4)$$

where

$$t_o = \sqrt{\frac{2md}{qE}} \left(\frac{2d+l}{2d} \right). \quad (5)$$

The measurable quantity t_o —obtained from Eq. (3)—corresponds to the flight time of electrons with $p_z=0$ (i.e., for trajectories that initially have no longitudinal momentum component).

The $p_z \ll \sqrt{2mqEd}$ approximation implies that the initial p_z momentum must be small compared to the momentum the electron has acquired at the exit of the electric field region. This condition can be formulated as $\varepsilon \ll qEd$, where ε is the electron’s initial kinetic energy; it can be satisfied if the energy acquired from the extraction field is relatively large with respect to ε . Otherwise the exact solution for p_z should be used (see Appendix A). It should be noted that the p_z determination depends only on the ability to measure time differences $(t-t_o)$ accurately, whereas $p_{x,y}$ depend on both the positional precision and the value of the overall time of flight. It is therefore convenient to separate the components x and y from z and to introduce the radial quantities $r = \sqrt{x^2 + y^2}$ and $p_r = \sqrt{p_x^2 + p_y^2}$; the radius r being the distance between the point of impact of the electron on the detector and the source point, which is taken to correspond to the center of the detector.

From the above equations, the electron kinetic energy, ε , is given by

$$\varepsilon = \frac{p_x^2 + p_y^2 + p_z^2}{2m} = \frac{m(x^2 + y^2)}{2t^2} + \frac{q^2 E^2}{2m} (t_o - t)^2. \quad (6)$$

Where possible, one should work in momentum space coordinates (p_x, p_y, p_z) , rather than using spherical angles $(\theta$ and $\phi)$ and energy (ε) . This stems from the fact that systematic and random errors, as expressed in spherical polar coordinates, are nonlinear. In addition, it introduces variable solid angles terms. These important aspects are often overlooked, especially when comparing data from these momentum-

mapping methods with those obtained by conventional energy- and angle-dispersive spectrometers (e.g., hemispherical, cylindrical, and toroidal analyzers).

In the situation that p_r equals the *total* momentum (i.e., $p_z=0$), which arises when $t=t_o$, r is denoted here as r_o [i.e., $r(t_o)=r_o$]. Equation (6) can therefore be expressed as

$$\varepsilon = \frac{mr_o^2}{2t_o^2}. \quad (7)$$

Note that in this case, r is maximized for a given energy ε . Hence in order to collect all electrons of a given kinetic energy, then r_o must be less than R , where R is the radius of the detector. It follows that the upper limit for kinetic energy collected over 4π can be deduced using Eqs. (5) and (7),

$$\varepsilon < \frac{R^2 q E d}{4} \left(\frac{2}{2d+l} \right)^2. \quad (8)$$

This limit depends on the geometry of the spectrometer. In particular, one should notice that it decreases as a function of the total length ($L=l+d$) of the TOF system.

If a uniform magnetic field, \mathbf{B} , is applied along the direction of the TOF axis, the electrons will experience the Lorentz force. The overall effect of the parallel \mathbf{E} and \mathbf{B} fields is a well-known helical or *spiral* trajectory. The coordinates x , y , and the radius $r=\sqrt{x^2+y^2}$ can be shown to be given by

$$x = \frac{1}{qB} p_y (1 - \cos(\omega t)) + \frac{1}{qB} p_x \sin(\omega t), \quad (9)$$

$$y = \frac{1}{qB} p_x (\cos(\omega t) - 1) + \frac{1}{qB} p_y \sin(\omega t), \quad (10)$$

$$r = \frac{2}{qB} \sqrt{p_x^2 + p_y^2} \left| \sin\left(\frac{\omega t}{2}\right) \right|, \quad (11)$$

where B is the strength of the magnetic field and ω , the cyclotron frequency, is expressed by

$$\omega = \frac{qB}{m}. \quad (12)$$

These equations reveal that the positions on the detector depend on the initial momenta (p_x, p_y), the magnitude of \mathbf{B} and the time of flight, which largely depends on the \mathbf{E} field strength for a fixed TOF geometry. Note also that the spiral axis is parallel to—but does not coincide with—the symmetry axis of the TOF (see Fig. 2). An interesting effect arising from the use of a \mathbf{B} field is seen in Eq. (11), namely that if $\omega t = n\pi$, where n is an even integer, then $r=x=y=0$ (see Figs. 2 and 3). The electrons arrive at the center of the detector and this is true regardless of p_x, p_y ; all electrons have performed an integer number of helical revolutions during the time of flight. The source point has been effectively “transferred” onto the detector. Therefore, the equation

$$\omega t = n\pi \quad (\text{even } n) \quad (13)$$

defines a set of “magnetic nodes.” By contrast if $\omega t = k\pi$, where k is an *odd* integer the radius reaches a maximum value, which is proportional to p_r/B . Furthermore, the radial dispersion with respect to p_r [i.e., $dr/dp_r \propto |\sin(\omega t/2)|$], see

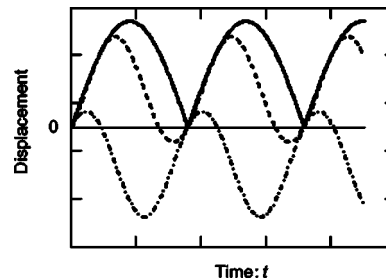


FIG. 2. Schematic diagram of (x, y) current position components, as a function of time, from $t=0$ to the time of arrival at the position-sensitive detector, for arbitrary values of p_x and p_y and of the electric and magnetic fields. The x (dashed), and y (dashed-dotted) values are shown along the same axis, together with $r=\sqrt{x^2+y^2}$ (solid curve), which corresponds to the radial extent of the trajectory at any given time. Notice that for this example the r -value returns to zero twice (within the displayed time range); this corresponds to “magnetic nodes,” as discussed in the text.

Eq. (11)] also reaches its maximum value, implying that optimal resolving power (i.e., a small change in p_r gives a largest possible change in radial position) is achieved when $\omega t = k\pi$. In practice, electrons of a given ε have a range of flight times. Since t_o is the mean t , the best overall resolution is obtained with $\omega t_o = k\pi$. Equation (11) conveniently illustrates the confinement of electrons due to the magnetic field with respect to the $\mathbf{B}=0$ situation described earlier, as r scales as $1/B$. Hence the magnetic field can be used to extend significantly the energy range of the system.

The expressions for x and y can be inverted, giving expressions for p_x , and p_y ,

$$p_x = \frac{qB}{2} \frac{\sin(\omega t)}{1 - \cos(\omega t)} x - \frac{qB}{2} y, \quad (14)$$

$$p_y = \frac{qB}{2} x - \frac{qB}{2} \frac{\sin(\omega t)}{1 - \cos(\omega t)} y. \quad (15)$$

First, note that Eq. (4) is still valid for the p_z component, as the \mathbf{B} field does not produce a force component in the z direction. Second, in contrast to Eqs. (1) and (2), p_x , and p_y now depend on both x and y . Finally note that Eqs. (14) and (15) reduce to Eqs. (1) and (2), respectively, in the case of $B \rightarrow 0$ (using the small angle approximations) as expected.

Combining Eqs. (4), (14), and (15), gives an expression for ε ,

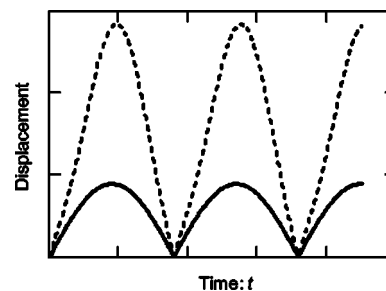


FIG. 3. Schematic diagram of the radial extent, $r=\sqrt{x^2+y^2}$, of trajectories for two different electron radial “energies” $[(p_x^2/2m) + (p_y^2/2m)]$, as a function of time. The dashed curve has $4\times$ the radial “energy,” of the solid curve. Notice that the r -values return to zero at the same time for both trajectories. As the time for the radial “collapse” is independent of electron energy, this is referred to as “magnetic nodes” in the text.

$$\varepsilon = \frac{q^2 B^2 (x^2 + y^2)}{4m(1 - \cos(\omega t))} + \frac{q^2 E^2}{2m} (t_o - t)^2. \quad (16)$$

As in Eq. (6), the first and second terms are due to the p_r and p_z contributions, respectively. Obviously, for any given energy, the contribution to ε from the first term is maximized when $p_z=0$, i.e., $t=t_o$. At this condition, where by definition $r=r_o$, Eq. (16) can also be formulated as

$$\varepsilon = \frac{q^2 B^2 r_o^2}{4m[1 - \cos(\omega t_o)]}. \quad (17)$$

As discussed above, in order to obtain the optimal resolving power, the following equation should be satisfied:

$$\omega t_o = k\pi \quad (18)$$

with k representing an *odd* integer. Since any deviation of t from t_o will now result in a smaller r , it follows that in this special case (i.e., $\omega t_o = k\pi$) r is maximized at $r=r_o$ for a given ε . Furthermore, this means electrons will be collected with 100% efficiency if $r_o < R$ (the size of the detector). Thus, for an (\mathbf{E}, \mathbf{B}) spectrometer, designed for optimal resolution, Eqs. (17) and (18) can be used to formulate a 4π sr collection criterion for ε ,

$$\varepsilon < \frac{q^2 B^2 R^2}{8m}. \quad (19)$$

This equation shows that the maximum kinetic energy depends only on B and R . Thus for a given detector size (R), there is a minimum value of B required which is independent of the \mathbf{E} field, as expected, since the motion along the spectrometer axis and perpendicular are not coupled by the magnetic field.

B. Treatment of magnetic nodes in an (\mathbf{E}, \mathbf{B}) spectrometer

As shown earlier, Eq. (13), defines a set of magnetic nodes, which are independent of p_x and p_y , i.e., the nodes prevent p_x and p_y being inferred. In this context, it is desirable to avoid magnetic nodes, but this is not always straightforward because electrons of a given energy ε have a range of time of flights. This time spread arises due to the different directions electrons may be emitted. The maximum range of their flight times is $\Delta t = t_{\text{back}} - t_{\text{for}}$, where t_{for} and t_{back} are the flight times for electrons emitted either directly towards or away from the detector.

In practice, it is possible to operate the TOF system in such a way as to encompass one or more magnetic nodes, rather than avoid them. This approach, however, has the consequent disadvantage that some E , θ , and ϕ combinations cannot be extracted from the data set. On the other hand, as it will be demonstrated, it allows the operation of lower extraction fields leading to higher turnaround times (Δt) [$\propto 1/E$, see Eq. (22)], which may be essential if the inherent time resolution (Δt_{min}) of the detection is poor, particularly in the case of a multiple particle coincidence experiment. Nevertheless, if the multi-hit capacity of the detector is good (with respect to Δt) it is worthwhile avoiding magnetic nodes and hence not surrendering any information that is required

for a “complete” experiment. Thus, this approach, which we will now pursue, allows all possible E , θ , and ϕ combinations to be extracted.

In our treatment therefore, the maximum kinetic energy that may be detected is restricted both by the requirements (a) that the electrons must be detected over 4π sr and (b) that the range of flight times (Δt) must be contained within two *adjacent* magnetic nodes. These two conditions in time restrict the choice of spectrometer geometry that can be used. The optimal experimental design parameters will be derived in the next two sections. If the interaction region is regarded as a point source, the TOF system should be designed so that these two limits occur at the same ε , the so called “point source optimal resolution” condition.

1. Containment of the electrons between two magnetic nodes

As previously reported,³³ the greatest likelihood of avoiding a “magnetic node” occurs when $\omega t_o = k\pi$ with k representing an *odd* integer, i.e., the spatial dispersion on the detector is largest. When B is selected so that $\omega t_o = k\pi$, all electrons of a given ε will be contained within the two adjacent magnetic nodes provided

$$\omega t_{\text{for}} > (k-1)\pi \quad \text{and} \quad \omega t_{\text{back}} < (k+1)\pi. \quad (20)$$

This condition leads to

$$\Delta t = t_{\text{back}} - t_{\text{for}} < \frac{2\pi m f}{qB}, \quad (21)$$

where we have introduced an additional “filling factor” $f < 1$, to be discussed below. When the electron is emitted forward and backward, $p_x = p_y = 0$ and $p_z = (2m\varepsilon)^{1/2}$. Within the same approximation as Eq. (4), Δt —the so-called “turn around” time—can be calculated using

$$\Delta t = \frac{2\sqrt{2m\varepsilon}}{qE}. \quad (22)$$

Combining Eqs. (21) and (22) leads directly to the upper limit for ε ,

$$\varepsilon < \frac{\pi^2 m E^2 f^2}{2B^2}. \quad (23)$$

The point source optimal resolution can be obtained by matching this limit with the criterion for 4π detection [Eq. (19)], which leads to

$$\frac{\pi^2 m E^2 f^2}{2B^2} = \frac{q^2 B^2 R^2}{8m} \quad (24)$$

and reduces to

$$R = \frac{2\pi E f}{qB^2}. \quad (25)$$

If the magnetic field, B , is selected according to Eq. (18), Eq. (25) is transformed to

$$R = \frac{2E t_o^2 q f}{m \pi k^2}. \quad (26)$$

Substituting Eq. (5) into Eq. (26) yields

$$R = \left(\frac{f}{k^2 \pi} \right) \left[\frac{(2d+l)^2}{d} \right] \quad (27)$$

which has one physical solution for l , namely

$$l = \sqrt{\pi d R k^2 / f} - 2d. \quad (28)$$

Thus for a given k , f , R , and d there is a unique value of l for which the two upper limits of ε [conditions (19) and (23)] coincide. Notice that this value is independent of both the magnetic and electric field strengths and the electron energy. Equations (27) and (28) define the ‘‘point source optimal resolution’’ condition. In practice if the filling factor f is nearly equal to 1 there may be considerable loss of resolution for electrons whose t is close to a magnetic node. Thus it is appropriate to impose that f must be significantly smaller than 1 (see Sec. III).

2. Space focusing

In reality the interaction region has a finite size and cannot be regarded as a point source of electrons. Hence ‘‘space focusing’’ should be incorporated to minimize the variation in t with respect to the electrons’ initial positions along the z axis.^{34,35} Minimizing variations in the measured values of x and y due to the extent of the source in the xy plane is not discussed here (see Refs. 33 and 36). Ideally the x , y source extent should be close to the detector’s spatial resolution limit ($\Delta x_{\min}, \Delta y_{\min}$).³⁷

It is well known³⁴ that for a one-field system such as that described above, first order space focusing can only be achieved for a single relationship between l and d , i.e.,

$$l = 2d. \quad (29)$$

Note that Eq. (29) is only valid for $p_z=0$. In the limit that $p_z \ll \sqrt{2mqEd}$, the p_z distribution is symmetric about $p_z=0$ and therefore it is appropriate to use $p_z=0$ for the space focusing condition.

If Eqs. (28) and (29) are to be satisfied simultaneously, then the extraction field length is constrained by

$$d = k^2 \left(\frac{\pi R}{16f} \right). \quad (30)$$

Thus if space focusing is to be implemented in addition to the point source optimal resolution condition (28), for given values of k , f , and R , the values for d and l are completely determined. Together with space focusing, Eq. (30) guarantees that a good matching of electric and magnetic fields can be found, taking full advantage of the detector size and allowing the complete analysis of all detected electrons. Note that the number of free parameters can be increased by moving to a two E -field spectrometer [Fig. 1(b)], the equations for which are given in Appendix B.

3. Choosing values for the free parameters

Equations (29) and (30) indicate that of the five TOF parameters, k (note that k can only take odd integer values), f ($f < 1$), R , d and l , only three can be independent. The choice of values for the three independent parameters (e.g., k , f , and R) should be made so as to achieve the best resolutions. The energy and angular resolutions are angle dependent and have a complicated analytic form that will not be

presented here. Numerically, plots of these resolutions are straightforward to generate and our final design parameters (see Sec. III) were chosen using such graphs. This being said, important insights into the problem can be gained using simple analytical expressions. For example, k , f , and R can be varied so as to maximize the *effective* positional and timing resolving powers, $R/\Delta R$ and $\Delta t/\Delta t_{\min}$. In these expressions, ΔR is a combination of the size of ‘‘channels’’ on the detector and the source dimension, while Δt_{\min} contains the detector’s inherent timing resolution and the pulse duration as already introduced. Clearly, the positional resolving power increases with the size of the detector (increasing R) and also with the density of ‘‘channels’’; reasonable dimensions of the physical detector and associated electronics provide an upper limit for these quantities. As for the timing resolving power, whilst Δt_{\min} is independent of the dimensions of the TOF system, Δt , the turnaround time, depends critically on R and f . Thus the values of these two parameters should be adjusted so as to maximize Δt . With the TOF system set up so as to satisfy the point source optimal resolution condition, it can be shown from Eqs. (18) and (24), that

$$\varepsilon_{\max} = \frac{f^2 E^2 q^2 t_o^2}{2k^2 m} = \frac{R^2 \pi^2 m k^2}{8t_o^2}, \quad (31)$$

where ε_{\max} is the maximum energy of electrons to be detected. It follows then that

$$E = \frac{4\varepsilon_{\max}}{fq\pi R}. \quad (32)$$

Substituting Eq. (32) into Eq. (22) allows Δt to be formulated in terms of R and f ,

$$\Delta t = \left(\frac{2m}{\varepsilon_{\max}} \right)^{0.5} \frac{f\pi R}{2}. \quad (33)$$

The implication of this expression is that although f has to be significantly lower than 1 to ensure all possible E , θ , and ϕ combinations can be extracted accurately (i.e., to ensure the radial dispersion with respect to p_r is large enough for all trajectories), too low an f value clearly has a detrimental effect on the overall resolution (as $\Delta t/\Delta t_{\min}$ becomes small). As a compromise between resolution and the accurate extraction of all information we operate at $f \sim 0.6$ (see Sec. III). As far as the detector size, R , is concerned it is clear that, as with positional resolution, good timing resolution is also favored by a large R value.

The final parameter, k , which does not appear in Eq. (33), is present explicitly in Eq. (30); thus the choice of k is dictated by the desired d and L [which are related by $L=d+l=3d$ from Eq. (29)]. A small value of L may be mechanically impractical whilst a large value presents the difficulty of maintaining a homogenous magnetic field over a long distance.

III. APPLICATION TO ‘‘CIEL’’

The original CIEL set up has been described in detail in a previous publication.¹⁵ In brief, the apparatus comprises two coaxial time-of-flight analyzers each fitted with a position-sensitive detector (see Fig. 4). A gaseous target is

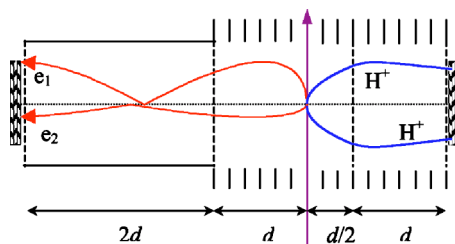
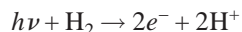


FIG. 4. (Color online) Diagram showing the modified TOF system used in the CIEL experiment for the investigation of H_2 double photoionization. The electron side was designed specifically to incorporate a coaxial magnetic field of $B=20$ Gauss. The upper trajectory corresponds to an electron of 23 eV emitted perpendicular ($\theta_1=90^\circ$) to the TOF axis. The lower trajectory shows an electron of complementary energy 2 eV (in a photo-double ionization experiment at 25 eV above threshold), emitted at $\theta_2=45^\circ$ towards the electron detector. The azimuthal angles of these electrons differ by 180° and the two trajectories belong to the plane of the figure. Note that although the two electrons return to the z axis at the same time, as already emphasized by Fig. 3, they do so at different positions.

ionized by synchrotron radiation, the resulting charged particles are extracted by a static electric field applied across the interaction region, the electrons traveling to one side and the ions to the other. Each of the detectors is equipped with a multi-hit capacity; thus the experiment is well suited to investigate multiple ionization processes and/or fragmentation of large molecules where the correlated measurement of several particles is required for a complete description. A parallel readout of the two detectors allows the correlation of electrons and ions. Our particular application concerned probing the photodouble ionization of H_2 ,



via the measurement of all four particles in coincidence. We wanted to work at 25 eV above threshold, near the peak of the double ionization total cross section yield, and detect electrons from 2 to 23 eV with acceptable resolution, in addition to the two ~ 10 eV protons. Such a momentum imaging study enables electron–electron correlations to be investigated in conjunction with the ions (i.e., in the molecular frame).

The electron time of flight analyzer was designed using a one-field scheme, with a detector size of $R=1.9$ cm and L could be chosen such that it was greater than 6 cm for mechanical reasons and less than 18 cm, resulting in $2\text{ cm} < d < 6$ cm. This upper limit on L was to comply with the requirement of maintaining a homogeneous magnetic field all along the electron trajectories by two coils of reasonable size (diameter of 1.2 m). For our initial experiments at Super-ACO the inherent timing resolution Δt_{min} equalled 1 ns, imposing a lower limit for the turnaround time, Δt , of at least 10 ns. Taking $R=1.9$ cm, $\varepsilon_{\text{max}}=23$ eV and $\Delta t \geq 10$ ns, Eq. (33) can be used to generate a lower limit to f of 0.5. One can take $f \leq 0.7$ as a practical upper limit for f , since f must be significantly less than 1 to avoid encompassing any magnetic nodes. Calculations using Eq. (30) show that these constraints on f and d can only be satisfied with $k=3$ and provided $f > 0.56$. Selecting $f=0.6$ as a reasonable compromise for the filling factor, d is determined to be 5.6 cm, corresponding to $\Delta t=12.6$ ns for the upper energy of 23 eV, from Eq. (33). From these design values of $k=3$, $f=0.6$, R

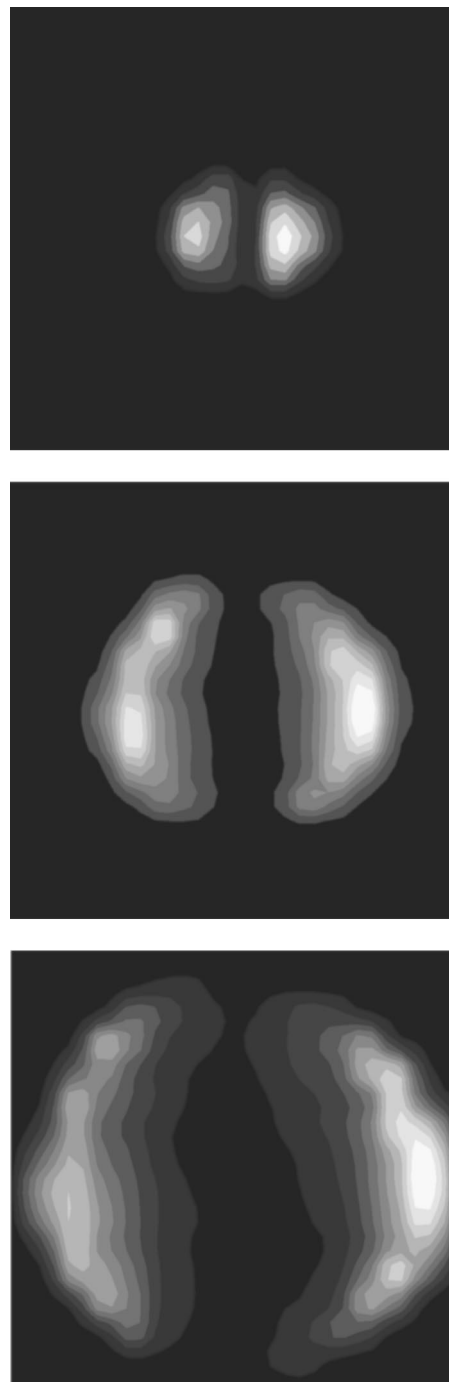


FIG. 5. Images on the position-sensitive detector for 2, 12, and 23 eV photoelectrons, arising from single photoionization of helium, showing the effect of magnetic confinement. Physically the polarization vector lies along the vertical direction of the figures, the effect of the magnetic field is to rotate the images by 90° , as discussed in the text.

$=1.9$ cm, $d=5.6$ cm, and $l=11.2$ cm we could derive $B=17$ G [from Eq. (19) with $\varepsilon_{\text{max}}=23$ eV], $E=26$ V cm $^{-1}$ [from Eq. (25)], and $t_o=31$ ns [from Eq. (18)].

Figure 5 shows a series of calibration spectra using single ionization of helium, as this results in photoelectrons of well-defined angular distributions (with asymmetry parameter $\beta=2$) to demonstrate that the inclusion of a magnetic field can be incorporated into such an instrument with no detrimental effects. These images exhibit two lobes in the direction perpendicular to the electric field, along which the

photoelectrons are emitted. This can be understood as, for the central time t_o , substituting Eq. (18) into Eqs. (9) and (10) leads to $y = -2p_x/qB$ and $x = +2p_y/qB$, i.e., a rotation by $\pi/2$ at the detector. The images increase in size due to the increasing photoelectron energy and the relatively large range of possible energies are a direct consequence of the magnetic confinement. Note that in the present conditions the values of p_z obtained from Eqs. (4) and (A11) are almost identical, which means that the assumed linear approximation holds very well. Using Eq. (4) then facilitates the analysis of electron momenta. The data reported in Fig. 5 were obtained at the Elettra synchrotron source (Trieste, Italy), using the detectors and electronics described by Lavollée.¹⁵ Under these conditions Δt_{\min} was estimated to be 0.5 ns and the angle and relative energy resolutions were typically 5° and 15%, respectively, for 12 eV electrons (middle image of Fig. 5). These performances can be improved by using (now available) faster electronics.

The electric field required by the electron side ($E = 26 \text{ V cm}^{-1}$) in the vicinity of the source point is too low for 4π collection of the 10 eV ions in a conventional TOF analyzer of realistic size. The conflicting demands of the electron and ion sides are usually overcome by employing pulsed electric fields. This approach, however, introduces significant complexities. In particular, it requires the use of sophisticated gating techniques (to inhibit and protect the detection electronics) and the technicalities with high field pulsing limits the maximum count rate (typically $<20 \text{ kHz}$). Instead we chose to switch from a conventional TOF analyzer to one that utilizes a weak (radially-symmetric) electric field in the drift region to generate a focusing electrostatic lens. This enables us to maintain a static field of 26 V cm^{-1} in the vicinity of the source point and collect all of the ions. The disadvantage of employing the radial focusing is that the ion images are less straightforward to analyze. Nevertheless, with a detailed numerical simulation of the weak lens incorporated into the data analysis, the use of such optics can become routine.

ACKNOWLEDGMENTS

D.P.S. and T.J.R. acknowledge EPSRC, University of Windsor, and NSERC for financial support. The authors are very grateful to E. Bouisset (LIXAM) for his contribution in adapting CIEL to the applied magnetic field, and to LURE for their financial support (Opération Spécifique).

APPENDIX A: EXACT SOLUTION FOR THE LONGITUDINAL MOMENTUM, p_z

We have shown that it is possible to determine the initial longitudinal momentum (p_z) by a simple measurement of the electron flight time [see Eq. (3)]. The solution to Eq. (3) is given by Eq. (4), which expresses a linear relationship between the longitudinal momentum (p_z), the electric field, and the measured time of flight. However, it should be kept in mind that the validity of this equation is restricted to the case where the initial p_z momentum is small compared to the momentum the electron has acquired at the exit of the electric field region.

In this section an exact solution of p_z for a one-field spectrometer is presented. The first region is considered to be the accelerating region of a length (d), and the second region is the field-free region of a length (l). Resolving the motion equations for the charged particle starting at $t=0$ and $z=0$, one can define t_1 as the time that it takes to reach the end of the first region, which satisfies the following condition:

$$d = \frac{qEt_1^2}{2m} + \frac{t_1}{m}p_z(t=0). \quad (\text{A1})$$

In the following we omit ($t=0$) in $p_z(t=0)$. In the second region, without an acceleration field, the quadratic term of the previous expression is absent, and we can define t_2 as

$$l = \frac{t_2}{m}p_z(t_1) = \frac{t_2}{m}(qEt_1 + p_z). \quad (\text{A2})$$

p_z from Eqs. (A1) and (A2) is given by

$$p_z = \frac{md}{t_1} - \frac{qEt_1}{2}, \quad (\text{A3})$$

$$p_z = \frac{ml}{t_2} - qEt_1. \quad (\text{A4})$$

Thus, a relationship between the electric field, the time of flights (t_1, t_2), and the geometric terms (l, d) can be found

$$\frac{qEt_1}{2} = \frac{ml}{t_2} - \frac{md}{t_1}. \quad (\text{A5})$$

This expression can be substituted into expression (A3) leading to

$$p_z = \frac{2md}{t_1} - \frac{ml}{t_2}. \quad (\text{A6})$$

Note that in the special case of $p_z=0$ one can derive from Eqs. (A5) and (A6),

$$t_1^0 = \left[\frac{2md}{qE} \right]^{1/2}, \quad (\text{A7})$$

where t_1^0 is the time of flight in the field region for this particular case. To the system of two Eqs. (A5) and (A6) with three unknown variables (p_z, t_1, t_2), a third equation $t_1+t_2=t$ introduces the *measured* total time of flight t . Hence, the problem is reduced to two equations and two unknown variables (p_z, t_1). An analytical solution of (t_1) can therefore be determined by rewriting Eq. (A5) as a third order polynomial

$$t_1^3 - t(t_1^2) + \frac{2m(l+d)}{qE}t_1 = \frac{2md}{qE}t. \quad (\text{A8})$$

The exact value for (t_1) is obtained as a root of such a polynomial from standard mathematics. By introducing

$$a = \frac{1}{27}t^3 - t(t_1^0)^2 \frac{l-2d}{6d}; \quad b = -\frac{1}{9}t^2 + \frac{1}{3}(t_1^0)^2 \frac{l+d}{d}. \quad (\text{A9})$$

For the $l=2d$ case, the quantity a^2+b^3 can be shown to be positive and hence the one real root of Eq. (A8) is given by

$$t_1 = \frac{1}{3}t + \sqrt[3]{a + \sqrt{a^2 + b^3}} + \sqrt[3]{a - \sqrt{a^2 + b^3}}. \quad (\text{A10})$$

Finally Eq. (A6) gives

$$p_z = \frac{2md}{t_1} - \frac{ml}{t - t_1} \quad (\text{A11})$$

allowing the exact value of p_z to be calculated.

APPENDIX B: EQUATIONS FOR POINT SOURCE OPTIMAL RESOLUTION CONDITION AND SPACE FOCUSING IN A TWO (ELECTRIC) FIELD TIME OF FLIGHT SYSTEM

In a two-field situation, the electrons are accelerated over distances, d_1 and d_2 , by electric fields, E_1 and E_2 , respectively. They subsequently move through a field-free region of length, l , before striking the position-sensitive detector of radius, R . To satisfy the basic point source optimal resolution condition, the TOF parameters must have the following relationship:

$$R = \left(\frac{4fd_1}{\pi k^2} \right) \left(\frac{1}{1 + \chi\alpha} \right) \left[\frac{\beta}{2} + \frac{1}{\chi}(1 + \chi\alpha) + \left(1 - \frac{1}{\chi} \right) \sqrt{1 + \chi\alpha} \right]^2, \quad (\text{B1})$$

where $\chi = E_2/E_1$, $\alpha = d_2/d_1$, and $\beta = l/d_1$. Thus there are seven TOF parameters ($R, f, k, \chi, d_1, \alpha, \beta$) of which six can be independently adjusted. The two-field situation is advantageous to the one-field case because Eq. (B1) contains χ , which can be varied after the apparatus is constructed. If, in addition, first-order space focusing is implemented, l is given by

$$l = 2d_1(1 + \chi\alpha) \left[\sqrt{1 + \chi\alpha} \left(1 - \frac{1}{\chi} \right) + \frac{1}{\chi} \right] \quad (\text{B2})$$

and the number of independent parameters drops to five. In the 2-field case, 2nd order space focusing may also be incorporated, if the interaction region is extensive in the z direction.

¹D. P. de Bruin and J. Los, Rev. Sci. Instrum. **53**, 1020 (1982).

²H. Helm and P. C. Crosby, J. Chem. Phys. **86**, 6813 (1987).

³Z. Vager, R. Naaman, and E. P. Kanter, Science **244**, 426 (1989)

⁴J. E. Pollard, D. A. Litchin, S. W. Janson, and R. B. Cohen, Rev. Sci. Instrum. **60**, 3171 (1989).

⁵J. H. D. Eland and A. H. Pearson, Meas. Sci. Technol. **1**, 36 (1990).

⁶J. E. Pollard, D. A. Litchin, S. W. Janson, and R. B. Cohen, Rev. Sci. Instrum. **61**, 3134 (1990).

⁷J. H. D. Eland, Meas. Sci. Technol. **5**, 1501 (1994).

⁸J. Becker, K. Beckford, U. Werner, and H. O. Lutz, Nucl. Instrum. Methods Phys. Res. A **337**, 409 (1994).

⁹R. Moshhammer, M. Unverzagt, W. Schmitt, J. Ullrich, and H. Schmidt-Böcking, Nucl. Instrum. Methods Phys. Res. B **108**, 425 (1996).

¹⁰N. Saito, F. Heiser, O. Hemmers, K. Wieliczek, J. Viehhaus, and U. Becker, Phys. Rev. A **54**, 2004 (1996).

¹¹Z. Amitay and D. Zajfman, Rev. Sci. Instrum. **68**, 1387 (1997).

¹²R. Dörner, V. Mergel, L. Spielberger, M. Achler, Kh. Khayyat, T. Vogt, H. Brauning, O. Jagutzki, T. Weber, J. Ullrich, R. Moshhammer, M. Unverzagt, W. Schmitt, H. Khemliche, M. H. Prior, C. L. Cocke, J. Feagin, R. E. Olson, and H. Schmidt-Böcking, Nucl. Instrum. Methods Phys. Res. B **124**, 225 (1997).

¹³H. Kollmus, W. Schmitt, R. Moshhammer, M. Unverzagt, and J. Ullrich, Nucl. Instrum. Methods Phys. Res. B **124**, 377 (1997).

¹⁴K. A. Hanold, A. K. Luong, T. G. Clements, and R. E. Continetti, Rev. Sci. Instrum. **70**, 2268 (1999).

¹⁵M. Lavollée, Rev. Sci. Instrum. **70**, 2968 (1999).

¹⁶H. B. Pedersen, M. J. Jensen, C. P. Safvan, X. Urbain, and L. H. Andersen, Rev. Sci. Instrum. **70**, 3289 (1999)

¹⁷I. Ali, R. Dörner, O. Jagutzki, S. Nuttgens, V. Mergel, L. Spielberger, Kh. Khayyat, T. Vogt, H. Brauning, K. Ullman, R. Moshhammer, J. Ullrich, S. Hagemann, K. O. Groeneveld, C. L. Cocke, and H. Schmidt-Böcking, Nucl. Instrum. Methods Phys. Res. B **149**, 490 (1999).

¹⁸D. Strasser, X. Urbain, H. B. Pedersen, N. Altstein, O. Heber, R. Wester, K. G. Bhushan, and D. Zajfman, Rev. Sci. Instrum. **71**, 3092 (2000).

¹⁹M. Braun, M. Beckert, and U. Müller, Rev. Sci. Instrum. **71**, 4535 (2000).

²⁰A. Lafosse, M. Lebeck, J. C. Brenot, P. M. Guyon, O. Jagutzki, L. Spielberger, M. Vervloet, J. C. Houver, and D. Doweck, Phys. Rev. Lett. **84**, 5987 (2000).

²¹A. Oelsner, O. Schmidt, M. Schicketanz, M. Klais, G. Schonhense, V. Mergel, O. Jagutzki, and H. Schmidt-Böcking, Rev. Sci. Instrum. **72**, 3968 (2001).

²²X. Flechard, C. Harel, H. Jouin, B. Pons, L. Adoui, F. Fremont, A. Cassimi, and D. Hennecart, J. Phys. B **34**, 2759 (2001).

²³A. I. Chichinin, T. Einfeld, C. Maul, and K. H. Gericke, Rev. Sci. Instrum. **73**, 1856 (2002).

²⁴M. Lebeck, J. C. Houver, and D. Doweck, Rev. Sci. Instrum. **73**, 1866 (2002).

²⁵M. Takahashi, T. Saito, M. Matsuo, and Y. Udagawa, Rev. Sci. Instrum. **73**, 2242 (2002).

²⁶L. Dinu, A. T. J. B. Eppink, F. Rosca-Pruna, H. L. Offerhaus, W. J. Van der Zande, and M. J. J. Vrakking, Rev. Sci. Instrum. **73**, 4206 (2002).

²⁷W. P. Hu, S. M. Harper, and S. D. Price, Meas. Sci. Technol. **13**, 1512 (2002).

²⁸S. N. Samarin, O. M. Artamonov, D. K. Waterhouse, J. Kirschner, A. Morozov, and J. F. Williams, Rev. Sci. Instrum. **74**, 1274 (2003).

²⁹J. J. Lin, J. Zhou, W. Shiu, and K. Liu, Rev. Sci. Instrum. **74**, 2495 (2003).

³⁰P. Michelato, L. Monaco, D. Sertore, and I. Pollini, Rev. Sci. Instrum. **74**, 2977 (2003).

³¹G. Laurent, M. Tarisien, X. Flechard, P. Jardin, L. Guillaume, P. Sobocinski, L. Adoui, A. Bordenave-Montesquieu, D. Bordenave-Montesquieu, J. Y. Chesnel, F. Fremont, D. Hennecart, E. Lienard, L. Maunoury, P. Moretto-Capelle, and A. Cassimi, Nucl. Instrum. Methods Phys. Res. B **205**, 546 (2003).

³²J. Ullrich, R. Moshhammer, R. Dörner, O. Jagutzki, V. Mergel, H. Schmidt-Böcking, and L. Spielberger, J. Phys. B **30**, 2917 (1997).

³³R. Dörner, V. Mergel, O. Jagutzki, L. Spielberger, J. Ullrich, R. Moshhammer, and H. Schmidt-Böcking, Phys. Rep. **330**, 95 (2000).

³⁴W. C. Wiley and I. H. McLaren, Rev. Sci. Instrum. **26**, 1150 (1955).

³⁵D. P. Seccombe and T. J. Reddish, Rev. Sci. Instrum. **72**, 1330 (2001).

³⁶A. T. J. B. Eppink and D. H. Parker, Rev. Sci. Instrum. **69**, 3477 (1997).

³⁷In certain special physical situations, the conservation of energy and momentum conditions can provide excess of information. It is therefore possible to utilize this to increase the number of experimental variables and still have kinematically complete results. It is thus possible to deduce the source point (x_s, y_s) of an event and not assume that it occurs at the origin (0,0). Consequently, even the effects of a finite source size can be accounted for.